ACS APPLIED MATERIALS & INTERFACES

www.acsami.org

Research Article

Slow-Released Cationic Redox Activity Promoted Stable Anionic Redox and Suppressed Jahn−Teller Distortion in Layered Sodium Manganese Oxides

Ao Zeng, Jianyue Jiao, Hong Zhang, Enyue Zhao,* Tao He, Zhenbang Xu, and Xiaoling Xiao*

Cite This: *ACS Appl. Mater. Interfaces* 2024, 16, 7119−7129

Read Online

ACCESS | Metrics & More | Article Recommendations | Supporting Information

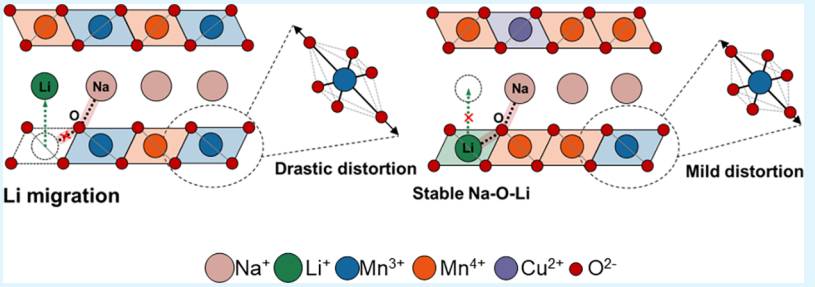

ABSTRACT: Manganese-based layered oxides are considered promising cathodes for sodium ion batteries due to their high capacity and low-cost manganese and sodium resources. Triggering the anionic redox reaction (ARR) can exceed the capacity limitation determined by conventional cationic redox. However, the unstable ARR charge compensation and Jahn−Teller distortion of Mn^{3+} ions readily result in structural degradation and rapid capacity fade. Here, we report a P2-type $Na_{0.8}Li_{0.2}Mn_{0.7}Cu_{0.1}O_2$ cathode that shows a capacity retention of 84.5% at 200 mA/g after 200 cycles. Combining *in situ* X-ray diffraction and multi other *ex situ* characterizations, we reveal that the enhanced cycling stability is ascribed to a slow release of cationic redox activity which can well suppress the Jahn−Teller distortion and favor the ARR reversibility. Furthermore, density-functional theory calculations demonstrate that the inhibited interlayer migration and reduced band gap facilitate the stability and kinetic behavior of ARR. These findings provide a perspective for designing high-energy-density cathode materials with ARR activity.

KEYWORDS: *sodium ion batteries, manganese-based layered oxide cathodes, anionic redox chemistry, Cu doping, Jahn−Teller effect*

1. INTRODUCTION

With the increased demand for new energy storage, the expansion of lithium-ion batteries (LIBs) industry has intensified the exploitation of limited lithium resources and their rising cost.[1−10] Sodium-ion batteries (SIBs) are considered a promising alternative to LIBs for energy storage due to their similar electrochemistry principle, rich sodium resources, and relatively low cost.[11−16] Developing high-performance cathode materials is one of the keys to further commercial applications of SIBs. Among the numerous cathode candidates reported so far, the layered transition metal (TM) oxides family (Na_xTMO_2), especially manganese-based layered oxides (Na_xMnO_2), have been deeply studied owing to their high theoretical capacity, extremely low cost, and environmental sustainability.[17−21] However, these layered Na_xMnO_2 compounds usually undergo serious MnO_6 octahedral distortion induced by the typical Jahn−Teller effect of high-spin Mn^{3+} ions during the electrochemical cycle, which results in structural deterioration and severe capacity fade.[22−24] To suppress the Jahn−Teller effect of the Mn^{3+} ion, various electrochemically inactive cationic ions (such as Mg^{2+}, Zn^{2+}, Al^{3+}, and Mo^{6+}) were introduced into TM ion sites to regulate the electron and band structure of MnO_6 octahedra.[25−28] Also, cationic B^{3+} ions with a small radius were introduced into the tetrahedral interstitial sites in the TM layer to effectively mitigate the Jahn−Teller effect.[29]

Although numerous modification approaches have been made to enhance the electrochemical properties of Na_xMnO_2 cathodes based on cationic TM ion redox, their energy density needs to be further improved for a practical energy storage system. Intriguingly, in addition to the conventional cationic redox, the oxygen-related anionic redox reaction (ARR) also participates in the charge compensation upon Na^+ ion extraction/intercalation to provide extra capacity and is therefore regarded as a new paradigm for designing high energy density cathodes.[30−32] Recently, some studies have

Received: October 31, 2023
Revised: January 10, 2024
Accepted: January 16, 2024
Published: January 31, 2024

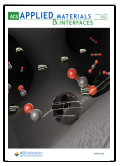

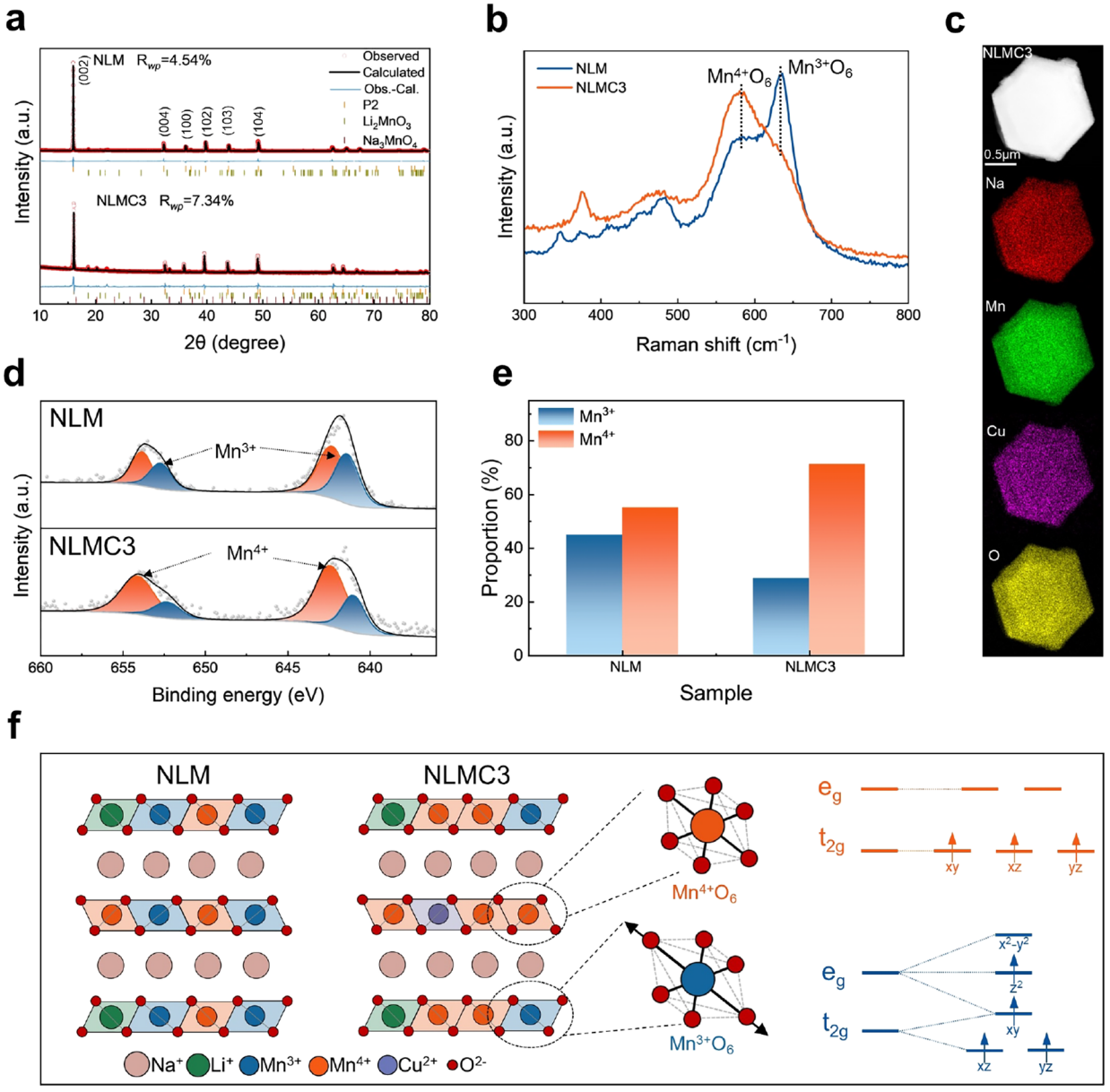

Figure 1. (a) Rietveld refinements of XRD data for the NLM and NLMC3 samples. (b) Raman spectra of NLM and NLMC3 samples. (c) TEM-EDS mapping spectra of the elements of the O, Na, Mn, and Cu elements for the NLMC3 sample. (d) Mn 2p XPS spectra and (e) corresponding proportion of Mn^{3+} and Mn^{4+} ions for NLM and NLMC3 samples. (f) Schematic illustration of P2-type layered structure for NLM and NLMC3 samples. The regular $Mn^{4+}O_6$ octahedra, distorted $Mn^{3+}O_6$ octahedra, and corresponding energy levels of the Mn-3d orbitals are shown schematically in detail.

demonstrated that $Na_x[A_yMn_{1-y}]O_2$ (A denotes Li, Mg, Zn, and vacancies) with nonbonding O 2p orbitals exhibits obvious ARR electrochemical behavior.[33−35] For instance, P3-type $Na_{0.6}[Li_{0.2}Mn_{0.8}]O_2$ cathode delivers a capacity of 75 mAh/g contributed by ARR at the high working voltage range.[36] P2-type $Na_{0.72}[Li_{0.24}Mn_{0.76}]O_2$ cathode delivers an ultrahigh capacity of 270 mAh/g beyond the theoretical limits.[37] However, the excessive ARR contributing high capacity induces irreversible charge compensation process, such as the formation of O_2^{2-} dimer or even oxygen release, which leads to the destruction of oxygen lattice structure and poor cycling performance.[38,39] To stabilize the ARR of $Na_x[A_yMn_{1-y}]O_2$ materials, many modification methods such as elemental doping/substitution and composition/structure adjustment have been employed.[40−44] For example, Mg and Ti dual doping strategy stabilizes the local structural environment and suppresses irreversible lattice oxygen loss to improve ARR stability.[45] In summary, $Na_x[A_yMn_{1-y}]O_2$ materials are trapped in the hesitant dilemma: (i) dual anionic and cationic redox reactions on capacity enhancement and (ii) Jahn−Teller effect of the Mn^{3+} ion and irreversible ARR on structural destruction. Therefore, a new strategy that simultaneously solves the above problems to achieve high capacity and long cycle performance is much desired.

Here, we present a low-cost and electrochemically active Cu^{2+} ion doping strategy that can tune cationic and anionic redox chemistry in P2-type $Na_{0.6+2x}Li_{0.2}Mn_{0.8-x}Cu_xO_2$ cathodes with significantly improved electrochemical performance. Specifically, the modified cathode exhibits an exceptional cycling process that the capacity gradually increases in the early

https://doi.org/10.1021/acsami.3c16320
ACS Appl. Mater. Interfaces 2024, 16, 7119−7129

stages and then basically maintains, achieving stable cycling performance with a capacity retention of 84.5% at 200 mA/g after 200 cycles. According to *in/ex situ* X-ray diffraction (XRD) and *ex situ* X-ray photoelectron spectroscopy (XPS), the slow-release activity of Mn^{3+}/Mn^{4+} redox not only gradually increases the capacity but also suppresses the distortion of MnO_6 octahedra. Meanwhile, a stable and highly active ARR is demonstrated by *ex situ* electron energy loss spectroscopy (EELS). Furthermore, density functional theory (DFT) calculations disclose that inhibited interlayer migration and reduced band gap are favorable for the stability and kinetic behavior of ARR. This work provides guidance for rationally designing high-energy-density cathode materials by simultaneously tuning cationic and anionic redox.

2. EXPERIMENTS AND METHODS

2.1. Materials Synthesis. A series of $Na_{0.6+2x}Li_{0.2}Mn_{0.8-x}Cu_xO_2$ (x = 0, 0.05, 0.075, 0.1) materials were synthesized via a solid-state reaction method and named NLM, NLMC1, NLMC2, and NLMC3 in turn. Na_2CO_3 (Macklin, 99.5%, 2% excess), Li_2CO_3(Sinopharm, AR, 2% excess), $MnCO_3$ (Macklin, Mn > 47%), and CuO (Macklin, 99%) in stoichiometric amounts were mixed and pressed into pellets under 3 MPa. The pellets were first calcined at 450 °C for 5 h (heating rate: 2 °C/min) and then 900 °C for 10 h (heating rate: 5 °C/min) in a muffle furnace (air atmosphere) and finally cooled naturally in a glovebox (argon atmosphere).

2.2. Material Characterizations. The crystal structures were studied by an X-ray diffractometer (XRD, Rigaku SmartLab) with Cu Kα radiation. Rietveld refinements of XRD data were performed with general structure and analysis system (GASA-II) software. Scanning electron microscopy (SEM, SU8020, Hitachi) equipped with an energy dispersive spectroscopy analyzer (EDS) and transmission electron microscopy (TEM, Tecnai G2 F30, FEI) were used to study morphological information. Binding energy was tested by X-ray photoelectron spectroscopy (XPS, ECSALAB 250Xi, Thermo Scientific). Electron energy loss spectroscopy (EELS) was measured by STEM (JEM-ARM200F, JEOL). For all *ex situ* characterizations, samples with different charge states were prepared in an argon atmosphere.

2.3. Electrochemical Measurements. The electrochemical performance was evaluated through the CR2032 coin cells. CR2032 coin cells were assembled in an argon-filled glovebox by using a prepared electrode as the cathode, a sodium metal piece as the anode, 1.0 M $NaClO_4$ in propylene carbonate/ethylene carbonate (PC/EC, 1:1) as the electrolyte, and a glass microfiber filter (GF/D, Whatman) as the separator. To fabricate the electrode, the homogeneous slurry made of 80 wt % active material, 10 wt % Super p carbon black, and 10 wt % polyvinylidene difluoride (PVDF) binder were distributed in *N*-methyl-pyrrolidone (NMP) to coat onto thin aluminum foils, followed by drying at 120 °C for 12 h in a vacuum. The mass loading of active material was about 1.5 mg/cm^2. Electrochemical measurement was performed on a battery testing system (CT-3008−5 V 10 mA, NEWARE). The C-rate is defined based on 1 C = 100 mA/g. Cyclic voltammetry (CV) curves was measured on an electrochemical workstation (PGSTAT302N, Metrohm).

2.4. Computational Details. All density-functional theory (DFT) computations were carried out using the Cambridge Sequential Total Energy Package based on the pseudopotential plane wave method. The electron−ion interactions were characterized using ultrasoft potentials. The wave functions were expanded by a plane wave basis set with a cutoff kinetic energy of 480 eV. The function parametrized by Perdew−Burke−Ernzerhof, a general gradient approximation, was used to describe the electron−electron exchange and correlation interactions. The van der Waals interactions were characterized by using the DFT-D2 method proposed by Grimme.

During the geometric optimization process, all atom sites were allowed to relax. Brillouin-zone integrations were performed using the special points of Monkhorst−Pack grids with a separation of 0.08 Å^{-1}. The convergence criterion of the electronic self-consistent field loop was set to 2 × 10^{-6} eV/atom. The atom structures have been optimized until the residual forces were below 0.05 eV/Å.

3. RESULTS AND DISCUSSION

3.1. Structural Characterizations. The crystal structures of the synthesized samples were analyzed using XRD (Figure S1). The main XRD peaks of all samples are indexed well to the P2-type layered structure (JCPDS card no. 27−0751) with the space group $P6_3/mmc$, which is consistent with the reported P2-type Na_xMnO_2 material.[24] The minor diffraction peak at 22° (2θ) is related to the ordered arrangement in the TM layer. The other diffraction peaks are mainly assigned to Li_2MnO_3 and Na_3MnO_4 impurity phases. Furthermore, Rietveld refinements were carried out to investigate the detailed crystal structure information, proving the introduction of the Cu^{2+} ion into the Mn site, as shown in Figure 1a, Figure S2, and Tables S1−S4. The total contents of these impurity phases (Table S5) are less than 3% in all samples; therefore, their effect on the electrochemical performance is negligible. The ICP results (Table S6) of the NLM and NLMC3 samples are in general agreement with the theoretical chemical composition. SEM images (Figure S3) show that all samples have similar sheetlike morphology with micrometer-sized particles, which proves that the introduction of Cu^{2+} ion has no impact on the morphology. TEM images (Figure S4) further show that NLM and NLMC3 have a typical hexagonal crystallite. The TEM-EDS (Figure 1c) and SEM-EDS (Figure S5) mappings demonstrate that Na, Mn, Cu, and O elements are uniformly distributed throughout the particles in all materials.

Raman peaks (Figure 1b) located near 480 and 600 cm^{-1} correspond to the in-plane O-TM-O bending modes and out-of-plane TM-O stretching modes, respectively, which are considered as the typical features of layered TM oxides.[46] The two intense signals located near 580 and 620 cm^{-1} are related to $Mn^{4+}O_6$ and $Mn^{3+}O_6$ octahedra, respectively. The valence state of Mn should be theoretically +4. The production of Mn^{3+} ions may be due to the inhomogeneous reaction process during actual synthesis. The relative intensity of I(620 cm^{-1})/I(580 cm^{-1}) is positively correlated with the ratio of Mn^{3+}/Mn^{4+} concentration, indicating a smaller Mn^{3+}/Mn^{4+} ratio in NLMC3.[47] Furthermore, the Mn 2p XPS spectra (Figure 1d) consist of both Mn^{3+} and Mn^{4+} signals.[48] The corresponding proportion of Mn^{3+} and Mn^{4+} ions estimated from the integrated area of peaks further proves that the content of Mn^{3+} ion decreased after the low-valent Cu^{2+} doping (Figure 1e).

Therefore, according to the characterization results presented above, the P2-type layered structure of NLM and NLMC3 is schematically provided in Figure 1f. Na^+ ions occupy the trigonal prismatic sites, Li^+, $Mn^{3+/4+}$, and Cu^{2+} ions are located in the octahedral sites in the TM layer, and the O^{2-} ions are stacked in the ABBA sequence. The structural differences between the $Mn^{3+}O_6$ octahedra and $Mn^{4+}O_6$ octahedra are worth noting. The Mn 3d orbitals split into bonding t_{2g} orbitals and antibonding e_g orbitals. The four 3d-electrons of high spin Mn^{3+} ion form t_{2g}^3-e_g^1 electronic configuration, which excites the Jahn−Teller effect and leads to the distorted $Mn^{3+}O_6$ octahedra. In contrast, the three 3d-electrons of Mn^{4+} ion form t_{2g}^3 electronic configuration and regular $Mn^{4+}O_6$ octahedra.[49] The crystal structure with a low

https://doi.org/10.1021/acsami.3c16320
ACS Appl. Mater. Interfaces 2024, 16, 7119−7129

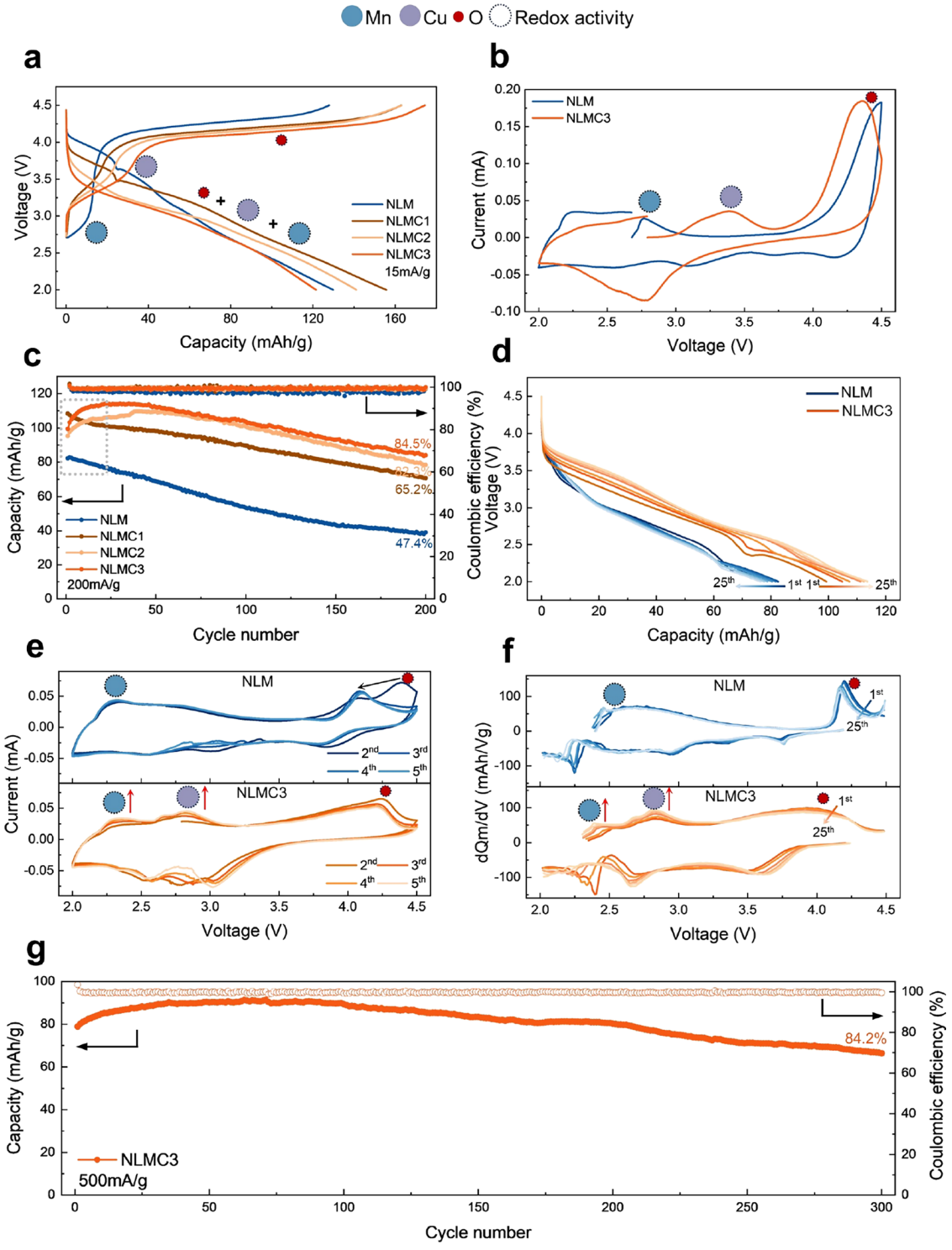

Figure 2. (a) Initial charge and discharge curves for NLM and NLMC1−3 samples between 2.0 and 4.5 V at a current density of 15 mA/g. (b) Initial CV curves (scanning rate: 0.1 mV/s) for NLM and NLMC3 samples. (c) Cycling performance for NLM and NLMC1−3 samples at 200 mA/g. (d) Discharge curves of NLM and NLMC3 samples in the initial 25 cycles. (e) CV curves (scanning rate: 0.1 mV/s) of NLM and NLMC3 samples in the initial 5 cycles. (f) dQ_m/dV curves of NLM and NLMC3 samples in the initial 25 cycles. (g) Long cycling performance of NLMC3 sample at 500 mA/g.

content of $Mn^{3+}O_6$ octahedra for NLMC3 suppresses Jahn−Teller distortion and thus exhibits high stability.

3.2. Electrochemical Properties. The initial galvanostatic charge and discharge curves (Figure 2a) of NLM and NLMC1−3 cathodes were tested between 2.0 and 4.5 V at a current density of 15 mA/g. For the NLM sample, the initial curves show an obvious two-step process with a steep slope area (~2.8 V) related to the cationic oxidation of Mn^{3+} to Mn^{4+} and a long platform area (above 4.0 V) related to the anionic oxidation (e.g., from O^{2-} to O^{-}/O_2^{2-}). For NLMC1−3 samples, the charge curves show the absence of the Mn^{3+} oxidation process, an additional slope area (~3.4 V) related to

https://doi.org/10.1021/acsami.3c16320
ACS Appl. Mater. Interfaces 2024, 16, 7119−7129

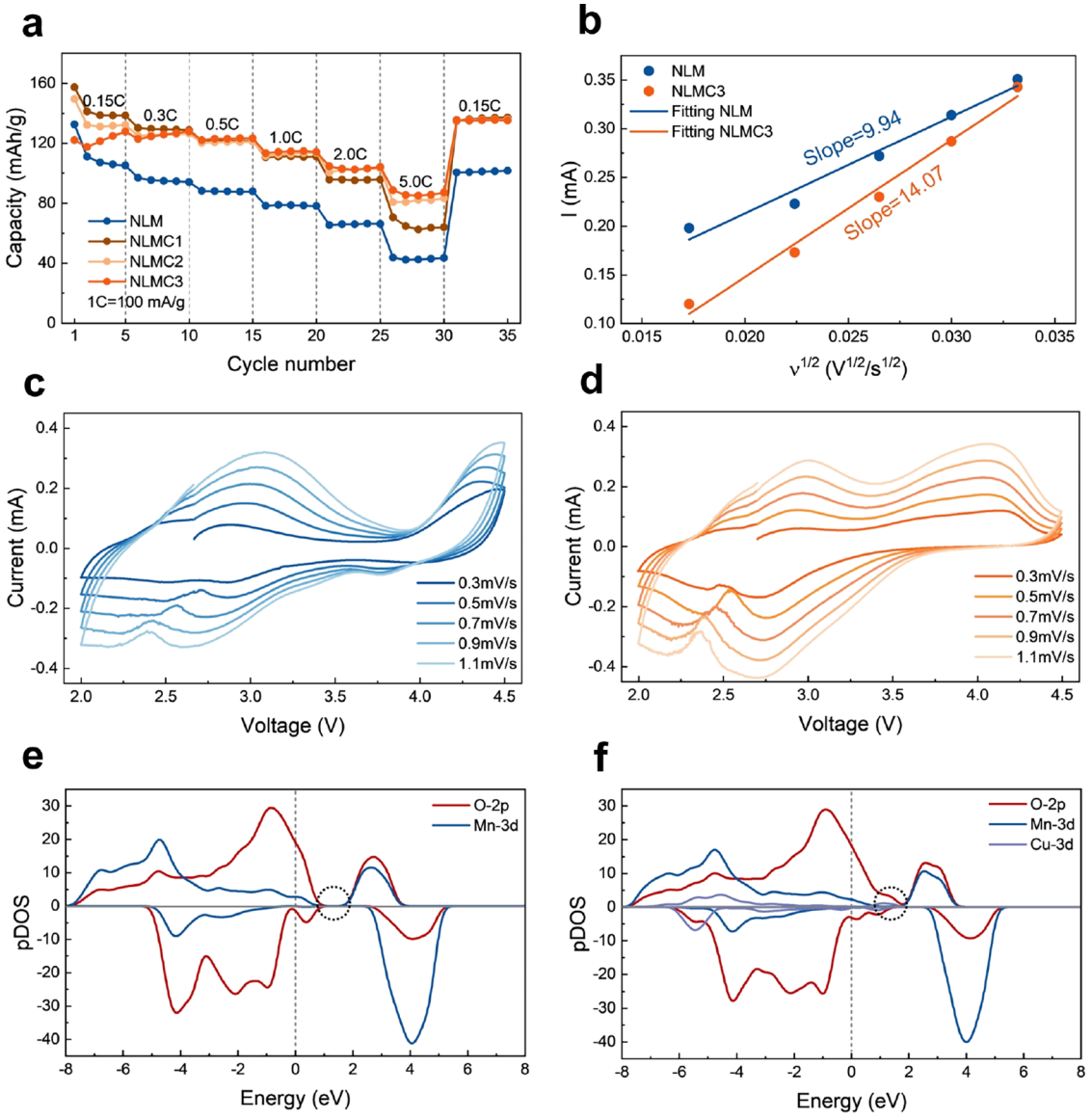

Figure 3. (a) Rate performance for NLM and NLMC1−3 samples between 2.0 and 4.5 V at various rates. (b) Linear fitting relationship between the peak value of the current and the square root of the scan rate derived from the CV curves in the range of 4.0−4.5 V. CV curves at different scan rates for (c) NLM and (d) NLMC3 electrodes. The pDOS calculations of the O 2p, Mn 3d, and Cu 3d orbitals for (e) NLM and (f) NLMC3 in the charged state.

oxidation of Cu^{2+} to Cu^{3+}, and a relatively lower anionic oxidation platform. The difference between the initial CV curves (Figure 2b) of NLM and NLMC3 can also support the above results. Similarly, the oxidation peaks at 2.8 and 4.5 V correspond to the oxidation of Mn^{3+} and O^{2-} ions for NLM, and the oxidation peaks at 3.4 and 4.3 V correspond to the oxidation of Cu^{2+} and O^{2-} ions for NLMC3. In addition, with the increase of doped Cu^{2+} ions, the oxidation process of the Cu^{2+} ion is more pronounced, and the anionic oxidation platform is lower and longer. These results indicate that more Cu^{2+} and O^{2-} ions are involved in the oxidation reaction to increase charge capacity, specifically from 128 to 174 mAh/g. The increase in Na^{+} ion content can also fully compensate for the above oxidation process. During the subsequent discharge process, NLMC1−3 shows the typically indistinguishable discharge curves because of the foggy boundary among the reduction processes of Mn^{4+}, Cu^{3+}, and O^{-}/O_2^{2-} ions. Compared with NLM, NLMC1 delivers a higher discharge capacity of 155 mAh/g, which is contributed by mixed anionic and cationic redox. However, as the substitution level of the Cu^{2+} ion increases to NLMC3, the discharge capacity gradually decreases, which may be caused by the inhibited activity of Mn^{3+}/Mn^{4+} redox.

The cycling performance was measured at a current of 200 mA/g in the voltage range 2.0−4.5 V, as shown in Figure 2c. At low amounts of Cu^{2+} ion substitution, NLMC1 shows higher capacity and better cycling performance than NLM. With a further increase in Cu^{2+} ion substitution, NLMC2 and NLMC3 exhibit the decreased initial discharge capacity and the gradually increasing discharge capacity in subsequent cycles. For example, compared with the NLM, the discharge capacity of NLMC3 increased from 99.3 to 113.6 mAh/g after 25 cycles and the detailed discharge curves are shown in Figure 2d. Furthermore, both the CV curves in the initial 5 cycles (Figure 2e) and the dQ_m/dV curves in the initial 25 cycles (Figure 2f) indicate that the intensity of Mn^{3+}/Mn^{4+} redox

https://doi.org/10.1021/acsami.3c16320
ACS Appl. Mater. Interfaces 2024, 16, 7119−7129

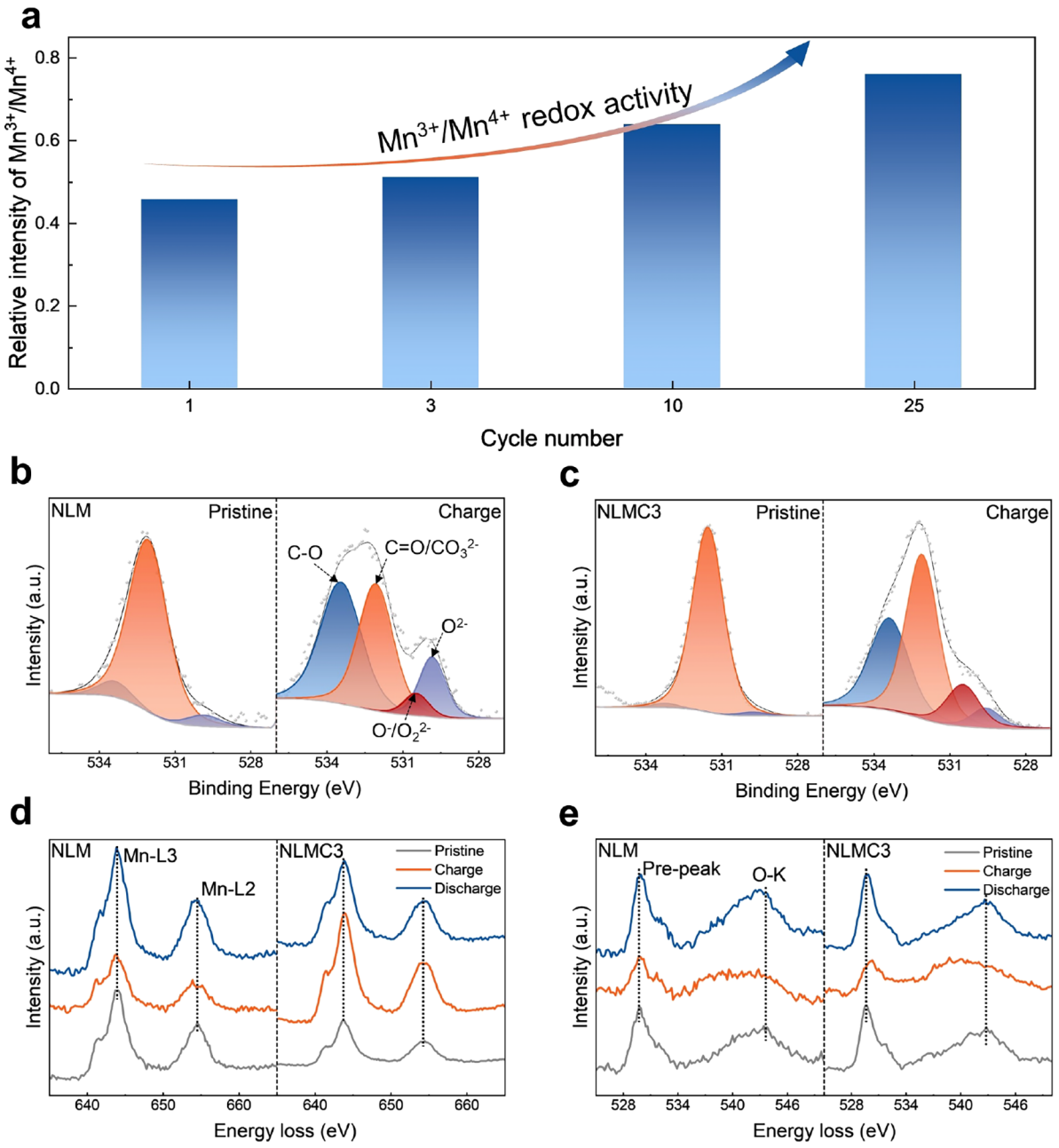

Figure 4. (a) Mn^{3+}/Mn^{4+} ratio for NLMC3 electrodes after the 1st, 3rd, 10th, and 25th cycles. *Ex situ* O 1s XPS spectra for (b) NLM and (c) NLMC3 at the state of pristine and charge to 4.5 V in the initial cycle. *Ex situ* EELS spectra of the (d) Mn L3-L2 edge and (e) the O K edge for NLM and NLMC3 at the state of pristine, charge to 4.5 V, and discharge to 2.0 V in the initial cycle.

peaks is maintained in NLM while the intensity of Mn^{3+}/Mn^{4+} and Cu^{2+}/Cu^{3+} redox peaks progressively increases (marked by red arrows) in NLMC3. These differentiated results suggest that Mn^{3+}/Mn^{4+} and Cu^{2+}/Cu^{3+} redox with gradually increasing activity contribute more capacity during cycling, which is the reason for the gradually increasing capacity of NLMC3. In addition, the highly overlapped CV curves above 4.0 V indicate the excellent ARR stability and stable oxygen lattice structure for NLMC3, while the dramatic shift of the oxidation peak to lower potential for NLM may be caused by the change of the lattice oxygen network due to $Mn^{3+}O_6$ octahedral distortion. Based on the above results, it can be assumed that a high level of Cu substitution can not only reduce the Mn^{3+} ion content of pristine sample to suppress the negative Jahn−Teller effect and stabilize crystal structure but also gradually and slowly release the Mn^{3+}/Mn^{4+} redox activity to improve the discharge capacity. Benefiting from these advantages, NLMC3 exhibits a high capacity retention of 104.2% after 100 cycles and 84.5% after 200 cycles (the retention is calculated based on the initial discharge capacity). Such an outstanding cycling performance is rare for P2-type cathodes with ARR in SIBs. Figure S6 shows that the average voltage is improved and further increases the energy density for all Cu-substituted samples because the potential of the Cu^{2+}/Cu^{3+} redox is higher than that of the Mn^{3+}/Mn^{4+} redox. The long cycling performance (Figure 2g) of the NLMC3 sample also exhibits little capacity decay at the high current density of 500 mA/g.

The rate performance was measured at rates from 0.15 to 5 C in the voltage range of 2.0−4.5 V, as shown in Figure 3a.

https://doi.org/10.1021/acsami.3c16320
ACS Appl. Mater. Interfaces 2024, 16, 7119−7129

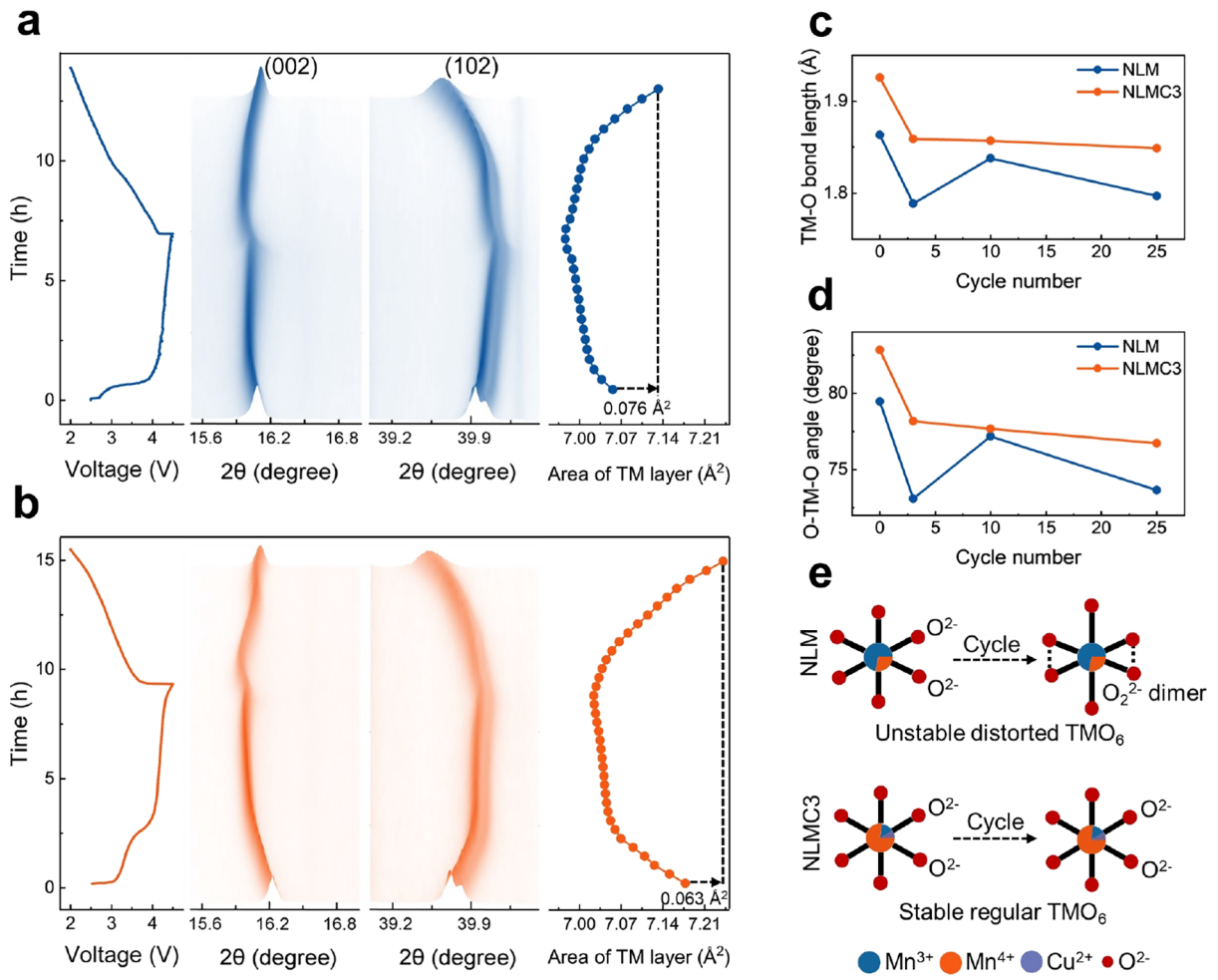

Figure 5. *In situ* XRD patterns and area evolution of the TM layer for (a) NLM and (b) NLMC3 electrodes in the initial cycle. The evolution of (c) the TM−O bond length and (d) the O−TM−O bond angle of TMO_6 octahedra for NLM and NLMC3 after the 3rd, 10th, and 25th cycles. (e) Schematic models of TMO_6 octahedral evolution for NLM and NLMC3.

The capacity of NLMC3 also increased gradually and reached 135 mAh/g after 35 cycles, which was higher than that of NLM. In addition, the rate performance of NLMC3 was significantly improved at high current density. As shown in Figure 3b−d, the related linear relationship between the peak value of the current and the square root of the scan rate derived from CV curves at different scan rates was performed to characterize the kinetic behavior for NLM and NLMC3. The Na^+ ion diffusion coefficient is calculated by the Randles−Sevcik equation (detailed calculations are shown in the Supporting Information). According to the fitting slope values derived from CV curves in the range of 4.0−4.5 V, the Na^+ ion diffusion coefficient of NLMC3 is larger than that of NLM in the oxidation process of the O^{2-} ion, implying that enhanced kinetic performance during ARR is related to the stable oxygen lattice structure. In addition, the partial density of states (pDOS) was further performed to study ARR behavior, as shown in Figure 3e,f. The electron-occupied states near the Fermi level are mostly dominated by the O 2p orbital, confirming the existence of the nonbonding O 2p orbital and the possibility of ARR. More importantly, the significant decrease in the band gap (marked by a circle) of the O 2p in NLMC3 indicates the enhanced charge transfer property of the O^{2-} ion, which is favorable for the kinetic behavior of ARR and rate performance.

3.3. Anionic and Cationic Redox Regulation. To investigate Mn-, Cu-, and O-related activities, the charge compensation mechanism was studied by XPS and EELS characterization techniques. *Ex situ* XPS spectra were tested for NLM and NLMC3 electrodes at the state of pristine, charged to 4.5 V, and discharged to 2.0 V in the initial cycle. Figure S7 and Table S7 summarize the Mn 2p spectra and the corresponding proportion of Mn^{3+} and Mn^{4+} ions. The change in the Mn^{3+}/Mn^{4+} ratio in different charge states proves the occurrence of Mn^{3+}/Mn^{4+} redox. The Mn 2p spectra of a series of charged and discharged electrodes under different cycles were tested for NLMC3, as shown in Figure S8. It can be seen from Figure 4a and Table S8 that the Mn^{3+}/Mn^{4+} ratio after the first, third, 10th, and 25th cycles is gradually increasing, which demonstrates the release and increase process for Mn^{3+}/Mn^{4+} redox activity. In addition, the O 1*s* spectra consist of C−O, C═O/CO_3^{2-}, peroxo-like species O^-/O_2^{2-} ion, and lattice oxygen O^{2-} ion, as shown in Figure 4b,c, Figure S9, and Table S9. The peak corresponding to O^-/O_2^{2-} ion near 530.5 V exhibits the appearance and disappearance in the charged and discharged states, respectively, proving the occurrence of ARR.[50] Compared to NLM, NLMC3 has a higher proportion of O^-/O_2^{2-} ion in the charged state, thus contributing more capacity, which is consistent with the results in Figure 2a. The O 1s spectra of the 25th cycle (Figure S10) is similar to that of

https://doi.org/10.1021/acsami.3c16320
ACS Appl. Mater. Interfaces 2024, 16, 7119−7129

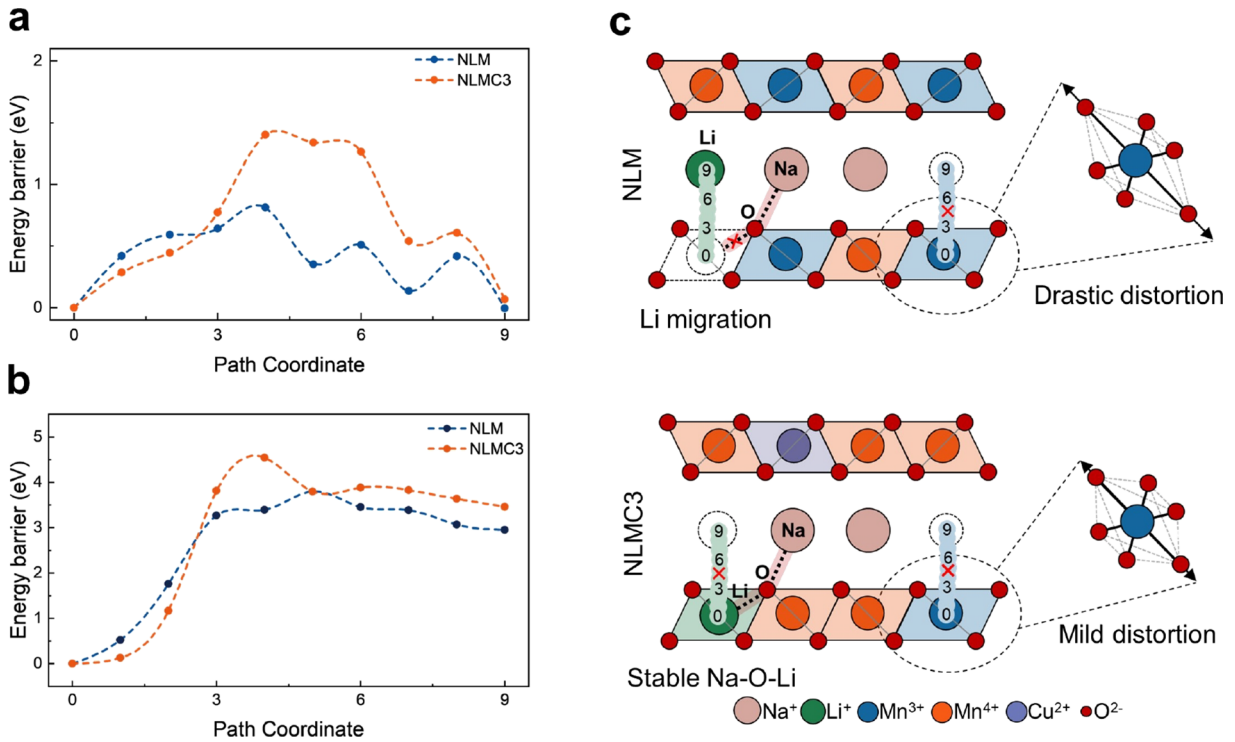

Figure 6. Energy barrier for the migration of (a) Li and (b) Mn from the TM layer to Na layer in NLM and NLMC3. (c) Schematic illustration of potential reaction mechanisms between NLM and NLMC3. The migration path is 0 → 3 → 6 → 9.

the initial cycle and also exhibits the obvious signal of O^-/O_2^{2-}, demonstrating the stability of ARR. Considering that XPS is only sensitive to near-surface information, it is not confirmed that the above results are also exhibited in the bulk. The electronic structure change of Mn, Cu, and O in the bulk at the state of pristine, charge to 4.5 V, and discharge to 2.0 V were further analyzed using EELS. Compared to NLM, the L3-L2 edge of the Mn EELS spectra (Figure 4d) in NLMC3 shows negligible changes, indicating the small contribution of inhibited Mn^{3+}/Mn^{4+} redox in the bulk.[51] The L3 edge of Cu (Figure S11) shifts high energy at the charged state and then reversibly shifts back to the initial position at the discharged state, demonstrating Cu^{2+}/Cu^{3+} redox. The shift of O pre-peak and K edge can reflect the O redox reaction.[52] Compared to NLM, the O K edge of NLMC3 (Figure 4e) undergoes a reversible shift process and the O pre-peak have larger energy variation, demonstrating a stable and highly active ARR.[53] Furthermore, the XANES energy shift values (Figure S12) of Mn K-edge and Cu K-edge for the NLMC3 electrode are larger in the 25th cycle than in the first cycle, also indicating the slow-released cationic redox activity.

3.4. Structural Evolutions. *In situ* XRD was measured to reveal the structural evolution of NLM and NLMC3 during the first cycle in the voltage range of 2.0−4.5 V. Figure 5a,b shows the charge and discharge curves and the evolution of the major diffraction peaks. In the charging process, the (002) diffraction peak shifts to a low angle, indicating an elongation of interlayer spacing along the *c*-axis caused by the increased electronic repulsive force between adjacent TMO_2 slabs during Na^+ ions deintercalation. After charging to 4.0 V, the shift of the (002) peak slows down significantly or even shifts back to a high angle, which is due to the loss of electrons in the oxidation reaction of the O^{2-} ions and thus the decreased interlayer O−O repulsive force. In contrast, the (102) peak shifts toward a higher angle, indicating the shrinkage of the *ab* plane or TM layer caused by the shortened TM−O distance during the oxidation of Cu^{2+}, Mn^{3+}, and O^{2-} ions.[54,55] In the subsequent discharging process, these peaks shift in opposite directions and eventually tend to return to their initial positions. During the whole process, the (002) and (102) peaks were retained, and no additional new peaks were detected. In addition, the effect of MnO_6 octahedral distortion on the TM layer is macroscopically reflected by the refined area evolution of TM layer. The area variations in the TM layer of NLMC3 before and after the first cycle is 0.063 $Å^2$, less than that of NLM (0.076 $Å^2$), implying the reversible structural evolution and regular TMO_6 octahedra in the TM layer. This result is caused by the suppressed Jahn−Teller effect and stable ARR in the NLMC3. The difference between the initial and final positions of (102) peak also supports the above view. Furthermore, to further investigate the structural evolution of TMO_6 octahedra in detail during the gradual increase of Mn^{3+}/Mn^{4+} redox activity, *ex situ* XRD measurements for NLM and NLMC3 after the 3rd, 10th, and 25th cycles were characterized. The corresponding refinement results are shown in Figure S13. Figure 5c,d shows the structural parameters of the TMO_6 octahedra for NLM and NLMC3 in detail. Obviously, the TMO_6 octahedra of NLMC3 has smaller and more stable fluctuations in structural parameters, including TM−O bond length and O−TM−O bond angle, indicating a stable and regular TMO_6 octahedra. As illustrated in Figure 5e, the TMO_6 octahedra of NLMC3 gradually adapt to mild Jahn−Teller distortion rather than suffering from severe and large-scale distortion of NLM, thus stabilizing the crystal structure in the electrochemical cycling process to some degree. Meanwhile, the longer TM−O bond and larger O−TM−O bond angle expand the distance between neighboring O^{2-} ions for NLMC3 and make it more difficult to form an unstable O_2^{2-}

https://doi.org/10.1021/acsami.3c16320
ACS Appl. Mater. Interfaces 2024, 16, 7119−7129

dimer, thus improving the stability of the oxygen lattice structure.

DFT calculations were further performed to study the structural stability. In the overall structure, the computational formation energy was further performed to evaluate the structure stability. The formation energy of the NLMC3 (−2.345 eV) structure model in the pristine state is lower than that of the NLM (−2.332 eV) structure model, suggesting a more stable crystal structure. The irreversible migration of partial TM ions from the TM layer into the Na layer leads to severe structural destruction and rapid capacity decay in Na_xTMO_2 cathodes. The interlayer migration of Li from the TM layer into the Na layer leads to dimerization of the O anions, which is detrimental to ARR stability. Therefore, suppressing the above interlayer migration is essential for the stability of cationic and anionic redox. Figure 6a,b shows the energy barriers for the interlayer migration of Li and Mn in NLM and NLMC3. For the Li migration, the negligible relative energy difference between initial and end positions and low energy barrier imply easy interlayer migration. Notably, the higher energy barrier in NLMC3 indicates the suppressed migration. The higher covalency of Cu−O bond compared with that of Mn−O is favorable for inhibiting the interlayer migration of Li.[56,57] In addition, based on Rietveld refinement of the XRD patterns (Tables S10 and S11), the refined Li occupancy of NLMC3 (0.18) after 25 cycles is higher than that of NLM (0.15), also indicating that the interlayer migration of Li was inhibited in NLMC3. For Mn migration, the extremely large energy difference and high energy barrier mean that Mn tends to stabilize in the TM layer rather than to migrate into the Na layer.

Therefore, combined with the above characterization results, the potential reaction mechanisms between NLM and NLMC3 are schematically shown in Figure 6c. The high content of the Mn^{3+} ion and high activity of Mn^{3+}/Mn^{4+} redox in NLM during cycling induce a drastic Jahn−Teller effect leading to distorted MnO_6 octahedra and an unstable oxygen lattice structure. More seriously, interlayer migration of Li disrupts the Na−O−Li configuration leading to the unstable ARR. In striking contrast to NLM, the low content of the Mn^{3+} ion in NLMC3 effectively inhibits the Jahn−Teller effect. The slow-release activity of Mn^{3+}/Mn^{4+} redox not only gradually increases the capacity but also allows MnO_6 octahedra to gradually adapt to mild distortion and thus maintain a stable crystal structure. Furthermore, the stabilized oxygen lattice structure and suppressed Li migration facilitate the stability of the ARR. Benefiting from the above modification mechanisms, NLMC3 stabilizes the cationic and anionic redox and achieves excellent electrochemical performance.

4. CONCLUSIONS

In this work, the P2-type NLMC3 cathode shows excellent electrochemical performance, maintaining 84.5% capacity retention at 200 mA/g after 200 cycles originating from stable cationic and anionic redox. Proved by multiple *in/ex situ* characterizations, cation-related Jahn−Teller distortion and anion-related irreversible behaviors have been suppressed by gradually releasing cationic activity and stable TMO_6 octahedra. In addition, DFT calculations also show that the inhibited interlayer migration and reduced bandgap facilitate the stability and kinetic behavior of ARR. This work not only emphasizes an effective strategy for simultaneously regulating cationic and anionic redox chemistry but also provides guidance for developing high-energy-density cathode materials in SIBs.

ASSOCIATED CONTENT

Supporting Information

The Supporting Information is available free of charge at https://pubs.acs.org/doi/10.1021/acsami.3c16320.

XRD patterns, SEM images, TEM images, mapping spectra, XPS spectra, XANES spectra, ICP, electrochemical performances, refined crystal structure parameters, and calculation of Na^+ ion diffusion coefficient (PDF)

AUTHOR INFORMATION

Corresponding Authors

Enyue Zhao − *Songshan Lake Materials Laboratory, Dongguan 523808, China;* orcid.org/0000-0003-4170-7427; Email: eyzhao@sslab.org.cn

Xiaoling Xiao − *College of Materials Science and Optoelectronic Technology, Center of Materials Science and Optoelectronics Engineering, University of Chinese Academy of Sciences, Beijing 100049, China;* orcid.org/0000-0002-9204-3715; Email: xlxiao@ucas.ac.cn

Authors

Ao Zeng − *College of Materials Science and Optoelectronic Technology, Center of Materials Science and Optoelectronics Engineering, University of Chinese Academy of Sciences, Beijing 100049, China*

Jianyue Jiao − *College of Materials Science and Optoelectronic Technology, Center of Materials Science and Optoelectronics Engineering, University of Chinese Academy of Sciences, Beijing 100049, China*

Hong Zhang − *College of Materials Science and Optoelectronic Technology, Center of Materials Science and Optoelectronics Engineering, University of Chinese Academy of Sciences, Beijing 100049, China*

Tao He − *Innovation Academy for Microsatellites of Chinese Academy of Sciences, Shanghai 201304, China*

Zhenbang Xu − *Changchun Institute of Optics, Fine Mechanics and Physics, Chinese Academy of Science, Changchun 130033, China*

Complete contact information is available at: https://pubs.acs.org/10.1021/acsami.3c16320

Notes

The authors declare no competing financial interest.

ACKNOWLEDGMENTS

This work was supported by the National Key R&D Program of China (grant no. 2022YFC2204502), the Fundamental Research Funds for the Central Universities, the National Natural Science Foundation of China (grant nos. 12105197 and 22379146), and Guangdong Basic and Applied Basic Research Foundation (grant no. 2022A1515010319). In addition, the authors thank Prof. Baotian Wang at Spallation Neutron Source Science Center for the technique help with DFT calculations.

REFERENCES

(1) Yabuuchi, N.; Hara, R.; Kajiyama, M.; Kubota, K.; Ishigaki, T.; Hoshikawa, A.; Komaba, S. New O2/P2-Type Li-Excess Layered

Manganese Oxides as Promising Multi-Functional Electrode Materials for Rechargeable Li/Na Batteries. *Adv. Energy Mater.* **2014**, *4* (13), 1301453.
(2) Hwang, J.-Y.; Myung, S.-T.; Sun, Y.-K. Sodium-Ion Batteries: Present and Future. *Chem. Soc. Rev.* **2017**, *46* (12), 3529−3614.
(3) Wu, K.; Ran, P.; Wang, S.; He, L.; Yin, W.; Wang, B.; Wang, F.; Zhao, J.; Zhao, E. Confining Bulk Molecular O_2 by Inhibiting Charge Transfer on Surface Anions toward Stable Redox Electrochemistry in Layered Oxide Cathodes. *Nano Energy* **2023**, *113*, No. 108602.
(4) Li, N.; Wang, S.; Zhao, E.; Yin, W.; Zhang, Z.; Wu, K.; Xu, J.; Kuroiwa, Y.; Hu, Z.; Wang, F.; Zhao, J.; Xiao, X. Tailoring Interphase Structure to Enable High-Rate, Durable Sodium-Ion Battery Cathode. *J. Energy Chem.* **2022**, *68*, 564−571.
(5) Zhang, B.; Zhao, Y.; Li, M.; Wang, Q.; Wang, X.; Cheng, L.; Ming, L.; Ou, X.; Wang, X. Amorphous Aluminum Oxide-Coated $NaFe_{0.33}Ni_{0.33}Mn_{0.33}O_2$ Cathode Materials: Enhancing Interface Charge Transfer for High-Performance Sodium-Ion Batteries. *ACS Appl. Mater. Interfaces* **2023**, 50994.
(6) Yi, X.; Rao, A. M.; Zhou, J.; Lu, B. Trimming the Degrees of Freedom via a K^+ Flux Rectifier for Safe and Long-Life Potassium-Ion Batteries. *Nano-Micro Lett.* **2023**, *15* (1), 200.
(7) Ma, X.; Fu, H.; Shen, J.; Zhang, D.; Zhou, J.; Tong, C.; Rao, A. M.; Zhou, J.; Fan, L.; Lu, B. Green Ether Electrolytes for Sustainable High-voltage Potassium Ion Batteries. *Angew. Chem., Int. Ed.* **2023**, *62* (49), No. e202312973.
(8) Zhang, Y.; Yi, X.; Fu, H.; Wang, X.; Gao, C.; Zhou, J.; Rao, A. M.; Lu, B. Reticular Elastic Solid Electrolyte Interface Enabled by an Industrial Dye for Ultrastable Potassium-Ion Batteries. *Small Struct.* **2024**, *5*, 2300232.
(9) Huang, Y. The Discovery of Cathode Materials for Lithium-ion Batteries from the View of Interdisciplinarity. *Interdiscip. Mater.* **2022**, *1* (3), 323−329.
(10) Zhang, L.; Liu, Y.; You, Y.; Vinu, A.; Mai, L. NASICONs-type Solid-state Electrolytes: The History, Physicochemical Properties, and Challenges. *Interdiscip. Mater.* **2023**, *2* (1), 91−110.
(11) Yabuuchi, N.; Kubota, K.; Dahbi, M.; Komaba, S. Research Development on Sodium-Ion Batteries. *Chem. Rev.* **2014**, *114* (23), 11636−11682.
(12) Xiao, Y.; Wang, P.-F.; Yin, Y.-X.; Zhu, Y.-F.; Yang, X.; Zhang, X.-D.; Wang, Y.; Guo, X.-D.; Zhong, B.-H.; Guo, Y.-G. A Layered-Tunnel Intergrowth Structure for High-Performance Sodium-Ion Oxide Cathode. *Adv. Energy Mater.* **2018**, *8* (22), 1800492.
(13) Liu, R.; Yang, L.; Wang, W.; Zhao, E.; Wang, B.; Zhang, X.; Liu, H.; Zeng, C. Surface Redox Pseudocapacitance-Based Vanadium Nitride Nanoparticles toward a Long-Cycling Sodium-Ion Battery. *Mater. Today Energy* **2023**, *34*, No. 101300.
(14) Jiao, J.; Wu, K.; Li, N.; Zhao, E.; Yin, W.; Hu, Z.; Wang, F.; Zhao, J.; Xiao, X. Tuning Anionic Redox Activity to Boost High-Performance Sodium-Storage in Low-Cost $Na_{0.67}Fe_{0.5}Mn_{0.5}O_2$ Cathode. *J. Energy Chem.* **2022**, *73*, 214−222.
(15) Yang, Q.; Wang, P.-F.; Guo, J.-Z.; Chen, Z.-M.; Pang, W.-L.; Huang, K.-C.; Guo, Y.-G.; Wu, X.-L.; Zhang, J.-P. Advanced P2-$Na_{2/3}Ni_{1/3}Mn_{7/12}Fe_{1/12}O_2$ Cathode Material with Suppressed P2−O2 Phase Transition toward High-Performance Sodium-Ion Battery. *ACS Appl. Mater. Interfaces* **2018**, *10* (40), 34272−34282.
(16) Jin, J.; Liu, Y.; Zhao, X.; Liu, H.; Deng, S.; Shen, Q.; Hou, Y.; Qi, H.; Xing, X.; Jiao, L.; Chen, J. Annealing in Argon Universally Upgrades the Na-Storage Performance of Mn-Based Layered Oxide Cathodes by Creating Bulk Oxygen Vacancies. *Angew. Chem., Int. Ed.* **2023**, *62* (15), No. e202219230.
(17) Luo, C.; Langrock, A.; Fan, X.; Liang, Y.; Wang, C. P2-Type Transition Metal Oxides for High Performance Na-Ion Battery Cathodes. *J. Mater. Chem. A* **2017**, *5* (34), 18214−18220.
(18) Ortiz-Vitoriano, N.; Drewett, N. E.; Gonzalo, E.; Rojo, T. High Performance Manganese-Based Layered Oxide Cathodes: Overcoming the Challenges of Sodium Ion Batteries. *Energy Environ. Sci.* **2017**, *10* (5), 1051−1074.
(19) Gao, A.; Zhang, Q.; Li, X.; Shang, T.; Tang, Z.; Lu, X.; Luo, Y.; Ding, J.; Kan, W. H.; Chen, H.; Yin, W.; Wang, X.; Xiao, D.; Su, D.; Li, H.; Rong, X.; Yu, X.; Yu, Q.; Meng, F.; Nan, C.; Delmas, C.; Chen, L.; Hu, Y.-S.; Gu, L. Topologically Protected Oxygen Redox in a Layered Manganese Oxide Cathode for Sustainable Batteries. *Nat. Sustain.* **2022**, *5* (3), 214−224.
(20) Ling, Y.; Zhou, J.; Guo, S.; Fu, H.; Zhou, Y.; Fang, G.; Wang, L.; Lu, B.; Cao, X.; Liang, S. Copper-Stabilized P′2-Type Layered Manganese Oxide Cathodes for High-Performance Sodium-Ion Batteries. *ACS Appl. Mater. Interfaces* **2021**, *13* (49), 58665−58673.
(21) Yang, T.; Huang, Y.; Zhang, J.; Zhu, H.; Ren, J.; Li, T.; Gallington, L. C.; Lan, S.; Yang, L.; Liu, Q. Insights into Ti Doping for Stabilizing the $Na_{2/3}Fe_{1/3}Mn_{2/3}O_2$ Cathode in Sodium Ion Battery. *J. Energy Chem.* **2022**, *73*, 542−548.
(22) Li, X.; Ma, X.; Su, D.; Liu, L.; Chisnell, R.; Ong, S. P.; Chen, H.; Toumar, A.; Idrobo, J.-C.; Lei, Y.; Bai, J.; Wang, F.; Lynn, J. W.; Lee, Y. S.; Ceder, G. Direct Visualization of the Jahn−Teller Effect Coupled to Na Ordering in $Na_{5/8}MnO_2$. *Nat. Mater.* **2014**, *13* (6), 586−592.
(23) Clément, R. J.; Bruce, P. G.; Grey, C. P. Review—Manganese-Based P2-Type Transition Metal Oxides as Sodium-Ion Battery Cathode Materials. *J. Electrochem. Soc.* **2015**, *162* (14), A2589−A2604.
(24) Zuo, W.; Qiu, J.; Liu, X.; Zheng, B.; Zhao, Y.; Li, J.; He, H.; Zhou, K.; Xiao, Z.; Li, Q.; Ortiz, G. F.; Yang, Y. Highly-Stable P2−$Na_{0.67}MnO_2$ Electrode Enabled by Lattice Tailoring and Surface Engineering. *Energy Storage Mater.* **2020**, *26*, 503−512.
(25) Clément, R. J.; Billaud, J.; Robert Armstrong, A.; Singh, G.; Rojo, T.; Bruce, P. G.; Grey, C. P. Structurally Stable Mg-Doped P2-$Na_{2/3}Mn_{1-y}Mg_yO_2$ Sodium-Ion Battery Cathodes with High Rate Performance: Insights from Electrochemical, NMR and Diffraction Studies. *Energy Environ. Sci.* **2016**, *9* (10), 3240−3251.
(26) Zhang, K.; Kim, D.; Hu, Z.; Park, M.; Noh, G.; Yang, Y.; Zhang, J.; Lau, V. W.; Chou, S.-L.; Cho, M.; Choi, S.-Y.; Kang, Y.-M. Manganese Based Layered Oxides with Modulated Electronic and Thermodynamic Properties for Sodium Ion Batteries. *Nat. Commun.* **2019**, *10* (1), 5203.
(27) Liu, X.; Zuo, W.; Zheng, B.; Xiang, Y.; Zhou, K.; Xiao, Z.; Shan, P.; Shi, J.; Li, Q.; Zhong, G.; Fu, R.; Yang, Y. P2-$Na_{0.67}Al_xMn_{1-x}O_2$: Cost-Effective, Stable and High-Rate Sodium Electrodes by Suppressing Phase Transitions and Enhancing Sodium Cation Mobility. *Angew. Chem., Int. Ed.* **2019**, *58* (50), 18086−18095.
(28) Zhang, L.; Wang, C.; Liu, Y.; Ren, M.; Du, J.; Chen, A.; Li, F. Suppressing Interlayer-Gliding and Jahn-Teller Effect in P2-Type Layered Manganese Oxide Cathode via Mo Doping for Sodium-Ion Batteries. *Chem. Eng. J.* **2021**, *426*, No. 130813.
(29) Fang, H.; Ji, H.; Zhai, J.; Wang, C.; Zhu, C.; Chen, G.; Chu, M.; Zhang, T.; Ma, Z.; Zhao, W.; Ji, W.; Xiao, Y. Mitigating Jahn−Teller Effect in Layered Cathode Material Via Interstitial Doping for High-Performance Sodium-Ion Batteries. *Small* **2023**, *19* (35), 2301360.
(30) Xu, H.; Guo, S.; Zhou, H. Review on Anionic Redox in Sodium-Ion Batteries. *J. Mater. Chem. A* **2019**, *7* (41), 23662−23678.
(31) Li, C.; Geng, F.; Hu, B.; Hu, B. Anionic Redox in Na-Based Layered Oxide Cathodes: A Review with Focus on Mechanism Studies. *Mater. Today Energy* **2020**, *17*, No. 100474.
(32) Jin, J.; Liu, Y.; Pang, X.; Wang, Y.; Xing, X.; Chen, J. A Comprehensive Understanding of the Anionic Redox Chemistry in Layered Oxide Cathodes for Sodium-Ion Batteries. *Sci. China Chem.* **2021**, *64* (3), 385−402.
(33) de la Llave, E.; Talaie, E.; Levi, E.; Nayak, P. K.; Dixit, M.; Rao, P. T.; Hartmann, P.; Chesneau, F.; Major, D. T.; Greenstein, M.; Aurbach, D.; Nazar, L. F. Improving Energy Density and Structural Stability of Manganese Oxide Cathodes for Na-Ion Batteries by Structural Lithium Substitution. *Chem. Mater.* **2016**, *28* (24), 9064−9076.
(34) Yabuuchi, N.; Hara, R.; Kubota, K.; Paulsen, J.; Kumakura, S.; Komaba, S. A New Electrode Material for Rechargeable Sodium Batteries: P2-Type $Na_{2/3}[Mg_{0.28}Mn_{0.72}]O_2$ with Anomalously High Reversible Capacity. *J. Mater. Chem. A* **2014**, *2* (40), 16851−16855.
(35) Zhao, C.; Wang, Q.; Lu, Y.; Jiang, L.; Liu, L.; Yu, X.; Chen, L.; Li, B.; Hu, Y.-S. Decreasing Transition Metal Triggered Oxygen

Redox Activity in Na-Deficient Oxides. *Energy Storage Mater.* **2019**, *20*, 395−400.
(36) Du, K.; Zhu, J.; Hu, G.; Gao, H.; Li, Y.; Goodenough, J. B. Exploring Reversible Oxidation of Oxygen in a Manganese Oxide. *Energy Environ. Sci.* **2016**, *9* (8), 2575−2577.
(37) Rong, X.; Hu, E.; Lu, Y.; Meng, F.; Zhao, C.; Wang, X.; Zhang, Q.; Yu, X.; Gu, L.; Hu, Y.-S.; Li, H.; Huang, X.; Yang, X.-Q.; Delmas, C.; Chen, L. Anionic Redox Reaction-Induced High-Capacity and Low-Strain Cathode with Suppressed Phase Transition. *Joule* **2019**, *3* (2), 503−517.
(38) House, R. A.; Maitra, U.; Jin, L.; Lozano, J. G.; Somerville, J. W.; Rees, N. H.; Naylor, A. J.; Duda, L. C.; Massel, F.; Chadwick, A. V.; Ramos, S.; Pickup, D. M.; McNally, D. E.; Lu, X.; Schmitt, T.; Roberts, M. R.; Bruce, P. G. What Triggers Oxygen Loss in Oxygen Redox Cathode Materials? *Chem. Mater.* **2019**, *31* (9), 3293−3300.
(39) Huang, Y.; Zhu, Y.; Nie, A.; Fu, H.; Hu, Z.; Sun, X.; Haw, S.; Chen, J.; Chan, T.; Yu, S.; Sun, G.; Jiang, G.; Han, J.; Luo, W.; Huang, Y. Enabling Anionic Redox Stability of P2-$Na_{5/6}Li_{1/4}Mn_{3/4}O_2$ by Mg Substitution. *Adv. Mater.* **2022**, *34* (9), 2105404.
(40) Yang, L.; Li, X.; Ma, X.; Xiong, S.; Liu, P.; Tang, Y.; Cheng, S.; Hu, Y.-Y.; Liu, M.; Chen, H. Design of High-Performance Cathode Materials with Single-Phase Pathway for Sodium Ion Batteries: A Study on P2-$Na_x(Li_yMn_{1-y})O_2$ Compounds. *J. Power Sources* **2018**, *381*, 171−180.
(41) House, R. A.; Maitra, U.; Pérez-Osorio, M. A.; Lozano, J. G.; Jin, L.; Somerville, J. W.; Duda, L. C.; Nag, A.; Walters, A.; Zhou, K.-J.; Roberts, M. R.; Bruce, P. G. Superstructure Control of First-Cycle Voltage Hysteresis in Oxygen-Redox Cathodes. *Nature* **2020**, *577* (7791), 502−508.
(42) Zeng, A.; Jiao, J.; Zhang, H.; Zhao, E.; Yin, W.; Wang, B.-T.; Xiao, X. Clarifying Effects of In-Plane Cationic-Ordering Degree on Anionic Redox Chemistry in Na-Ion Battery Layered Oxide Cathodes. *Mater. Today Chem.* **2023**, *30*, No. 101532.
(43) Wang, Y.; Zhao, X.; Jin, J.; Shen, Q.; Hu, Y.; Song, X.; Li, H.; Qu, X.; Jiao, L.; Liu, Y. Boosting the Reversibility and Kinetics of Anionic Redox Chemistry in Sodium-Ion Oxide Cathodes via Reductive Coupling Mechanism. *J. Am. Chem. Soc.* **2023**, *145* (41), 22708−22719.
(44) Shen, Q.; Liu, Y.; Zhao, X.; Jin, J.; Song, X.; Wang, Y.; Qu, X.; Jiao, L. Unexpectedly High Cycling Stability Induced by a High Charge Cut-Off Voltage of Layered Sodium Oxide Cathodes. *Adv. Energy Mater.* **2023**, *13* (6), 2203216.
(45) Rahman, M. M.; McGuigan, S.; Li, S.; Gao, L.; Hou, D.; Yang, Z.; Xu, Z.; Lee, S.-J.; Sun, C.-J.; Liu, J.; Huang, X.; Xiao, X.; Chu, Y.; Sainio, S.; Nordlund, D.; Kong, X.; Liu, Y.; Lin, F. Chemical Modulation of Local Transition Metal Environment Enables Reversible Oxygen Redox in Mn-Based Layered Cathodes. *ACS Energy Lett.* **2021**, *6* (8), 2882−2890.
(46) Ouyang, B.; Chen, T.; Chen, X.; Fan, X.; Wang, J.; Liu, W.; Lu, Z.; Liu, K. Construction of Co/Ni-Free P2-Layered Metal Oxide Cathode with High Reversible Oxygen Redox for Sodium Ion Batteries. *Chem. Eng. J.* **2023**, *452*, No. 138912.
(47) Hwang, S.-J.; Park, D.-H.; Choy, J.-H.; Campet, G. Effect of Chromium Substitution on the Lattice Vibration of Spinel Lithium Manganate: A New Interpretation of the Raman Spectrum of $LiMn_2O_4$. *J. Phys. Chem. B* **2004**, *108* (34), 12713−12717.
(48) Li, S.; Wu, L.; Fu, H.; Rao, A. M.; Cha, L.; Zhou, J.; Lu, B. Entropy-Tuned Layered Oxide Cathodes for Potassium-Ion Batteries. *Small Methods* **2023**, *7* (11), 2300893.
(49) Liu, Y.; Wang, C.; Zhao, S.; Zhang, L.; Zhang, K.; Li, F.; Chen, J. Mitigation of Jahn−Teller Distortion and Na^+/Vacancy Ordering in a Distorted Manganese Oxide Cathode Material by Li Substitution. *Chem. Sci.* **2021**, *12* (3), 1062−1067.
(50) McCalla, E.; Abakumov, A. M.; Saubanère, M.; Foix, D.; Berg, E. J.; Rousse, G.; Doublet, M.-L.; Gonbeau, D.; Novák, P.; Van Tendeloo, G.; Dominko, R.; Tarascon, J.-M. Visualization of O-O Peroxo-like Dimers in High-Capacity Layered Oxides for Li-Ion Batteries. *Science* **2015**, *350* (6267), 1516−1521.
(51) Zheng, W.; Liu, Q.; Wang, Z.; Wu, Z.; Gu, S.; Cao, L.; Zhang, K.; Fransaer, J.; Lu, Z. Oxygen Redox Activity with Small Voltage Hysteresis in $Na_{0.67}Cu_{0.28}Mn_{0.72}O_2$ for Sodium-Ion Batteries. *Energy Storage Mater.* **2020**, *28*, 300−306.
(52) Wang, C.; Liu, L.; Zhao, S.; Liu, Y.; Yang, Y.; Yu, H.; Lee, S.; Lee, G.-H.; Kang, Y.-M.; Liu, R.; Li, F.; Chen, J. Tuning Local Chemistry of P2 Layered-Oxide Cathode for High Energy and Long Cycles of Sodium-Ion Battery. *Nat. Commun.* **2021**, *12* (1), 2256.
(53) Li, N.; Zhao, E.; Zhang, Z.; Yin, W.; Wang, B.-T.; Xiao, X. De-Clustered Nonbonding Oxygen State Inhibits Oxygen Dimerization for Highly Activated and Stable Anionic Redox in Sodium-Based Layered Cathodes. *Chem. Eng. J.* **2023**, *466*, No. 143145.
(54) Xiao, Y.; Zhu, Y.; Yao, H.; Wang, P.; Zhang, X.; Li, H.; Yang, X.; Gu, L.; Li, Y.; Wang, T.; Yin, Y.; Guo, X.; Zhong, B.; Guo, Y. A Stable Layered Oxide Cathode Material for High-Performance Sodium-Ion Battery. *Adv. Energy Mater.* **2019**, *9* (19), 1803978.
(55) Cheng, C.; Chen, C.; Chu, S.; Hu, H.; Yan, T.; Xia, X.; Feng, X.; Guo, J.; Sun, D.; Wu, J.; Guo, S.; Zhang, L. Enhancing the Reversibility of Lattice Oxygen Redox Through Modulated Transition Metal−Oxygen Covalency for Layered Battery Electrodes. *Adv. Mater.* **2022**, *34* (20), 2201152.
(56) Allred, A. L. Electronegativity Values from Thermochemical Data. *J. Inorg. Nucl. Chem.* **1961**, *17* (3−4), 215−221.
(57) Voronina, N.; Shin, M.; Kim, H.; Yaqoob, N.; Guillon, O.; Song, S. H.; Kim, H.; Lim, H.; Jung, H.; Kim, Y.; Lee, H.; Lee, K.; Yazawa, K.; Gotoh, K.; Kaghazchi, P.; Myung, S. Hysteresis-Suppressed Reversible Oxygen-Redox Cathodes for Sodium-Ion Batteries. *Adv. Energy Mater.* **2022**, *12* (21), 2103939.

https://doi.org/10.1021/acsami.3c16320
ACS Appl. Mater. Interfaces 2024, 16, 7119−7129